Applied Physics A (2026) 132:530
https://doi.org/10.1007/s00339-026-09735-4

Applied Physics A
Materials Science & Processing

Optoelectronic performance of Au/FMDD/p-Si/Al structure: photodiode and photovoltaic analysis

Ali Rıza Deniz[1] · Musa Erdoğan[2,3] · Zakir Çaldıran[4] · Gökhan Gök[5] · Erbay Kalay[6]

Received: 18 February 2026 / Accepted: 17 May 2026 / Published online: 22 May 2026
© The Author(s) 2026

Abstract

In this study, to improve the performance of conventional silicon (Si)-based optoelectronic devices, an Au/FMDD/p-Si/Al Metal-Interlayer-Semiconductor (MIS) structure was successfully fabricated by introducing a new organic interlayer material at the metal-semiconductor interface. In this context, a new fluorene-based aldodioxime derivative, (1E,1'E)-4,4'-((9*H*-fluoren-9-ylidene)methylene)dibenzaldehyde dioxime (FMDD), was designed, synthesized, and spectroscopically characterized. The target compound was successfully obtained in three steps-bromination, Suzuki coupling, and condensation reactions-starting from commercially available 9*H*-fluoren-9-one (**1**). The structure of the product was confirmed by ^{1}H NMR, ^{13}C NMR, and MS analyses. The morphological, structural and optical properties of the FMDD interlayer film were investigated in detail by SEM, AFM, XRD and UV-Vis analyses. The analyses revealed that the FMDD film was not amorphous but had a nanogranular (20–50 nm) crystalline structure and a rough surface. Optical analysis confirmed that FMDD has a wide band gap of ~2.25 eV and exhibits high optical transparency to visible/near-infrared light above 550 nm. The electrical properties (I-V) of the device were investigated under darkness and illumination. In darkness, the diode exhibited good rectifying characteristics with an ideality factor (n) of 1.21 and a rectification ratio (RR) of 144.3. However, under illumination, the series resistance (R_s) increased sharply up to 3386 Ω and n increased to 3.14, severely limiting the photovoltaic performance of the device. Consequently, the device exhibited a very low fill factor (FF ~ 22.9%) and a maximum efficiency (η) of 0.34%. Analyses performed in photodiode mode (under V = -2 V) revealed a much more interesting behavior: the photocurrent (I_{ph}), photosensitivity (S), and detectability (D^*) of the device remained constant at low levels up to 60 mW/cm² light intensity, but showed a sharp and sudden increase above this threshold. This superlinear behavior was attributed to a photoconductive mechanism triggered by the saturation of the trap states at the interface under high photon flux. These results indicate that the FMDD interlayer is a potential candidate for achieving nonlinear and tunable photoresponse properties in Si-based devices.

Keywords Fluorene · Aldodioxime · P-Si hybrid diode · Photodiode · Photovoltaic · Photosensitivity · Dedectivity

✉ Ali Rıza Deniz
alirizadeniz@hakkari.edu.tr

✉ Musa Erdoğan
musaerdogan0@gmail.com

[1] Department of Electric and Energy, Çölemerik V.H.S, Hakkari University, Hakkari, Türkiye

[2] Department of Industrial Engineering, Faculty of Engineering and Architecture, Kafkas University, Kars, Türkiye

[3] Department of Food Engineering, Faculty of Engineering and Architecture, Kafkas University, Kars, Türkiye

[4] Department of Electric and Energy, Tech. Sci. V.H.S, Ardahan University, Ardahan, Türkiye, Turkey

[5] Department of Material Science and Engineering, Faculty of Engineering, Hakkari University, Hakkâri, Turkey

[6] Kars Vocational School, Department of Material and Material Processing Technologies, Kafkas University, Kars, Turkey

1 Introduction

Silicon (Si), the cornerstone of semiconductor technology, has dominated the electronics industry for decades thanks to its low cost, abundance, compatibility with industrial processes, and environmental stability. In addition to electronic applications, silicon-based structures continue to be the primary material for critical components such as photodetectors, image sensors, and solar cells in optoelectronics [1, 2]. While traditional silicon p-n junctions are widely used in this field, Metal-Semiconductor (MS) Schottky diodes and Metal-Insulator-Semiconductor (MIS) structures have attracted considerable attention due to their advantages such as faster response times, simpler fabrication processes, and low-temperature fabrication [3]. However, the fabrication of ideal Schottky contacts (MS) is challenging, and these structures often face issues such as high reverse leakage currents and high interfacial density of states, which limit their performance [4]. To overcome these limitations, intentionally placing a thin insulator or a wide bandgap interlayer between the metal and the semiconductor has been proven as an effective interfacial engineering strategy [5, 6].

This interlayer can significantly reduce the leakage current by preventing direct tunneling, prevent Fermi level locking (pinning) by passivating the interface states, and improve the electrical and optoelectronic properties of the device by modulating the effective barrier height [7]. For this purpose, traditional inorganic dielectrics such as SiO_2, Si_3N_4, HfO_2 and Al_2O_3 have been widely used [8, 9]. However, in recent years, organic materials offering ease of fabrication, low cost, tunable chemical/physical properties, and flexible device compatibility have attracted great interest for use as interlayers in WBI structures [10, 11]. These organic materials play a key role in the development of inorganic/organic hybrid optoelectronic devices.

Among organic molecules, fluorene-a member of the vast family of organic compounds-is a rigid, planar, polycyclic aromatic hydrocarbon with the molecular formula $(C_6H_4)_2CH_2$. Its white crystalline form exhibits a characteristic violet fluorescence, from which the compound derives its name. Fluorene displays a combination of remarkable photophysical attributes, including high solubility, photostability, a large two-photon absorption (2PA) cross-section, and an intrinsically functionalizable molecular framework. These features endow fluorene with significant advantages over other polyaromatic scaffolds such as stilbene, pyrene, and naphthalene [12, 13]. In particular, the enhanced rigidity of the fluorene core confers superior planarity and extended π-conjugation compared to stilbenyl analogues [14]. Organic molecules incorporating the fluorene backbone have attracted broad scientific interest owing to the unique photophysical and chemical characteristics of this motif [15]. Extensive literature reports highlight the widespread use of fluorene derivatives in materials science and optoelectronics, particularly in optical and three-dimensional data storage, organic light-emitting diodes (OLEDs), dye-sensitized solar cells (DSSCs), and nonlinear optical materials designed for telecommunication technologies [12–16]. Oximes are widely employed in the design of chemical sensors, bioimaging probes, organocatalysts, and coordination complexes owing to their facile preparation from carbonyl compounds and the strong coordinating ability of the oxime functional group toward both metal ions and anions [17]. When integrated into π-conjugated systems-such as pyrene or other aromatic frameworks-oxime derivatives exhibit remarkable photostability, high two-photon absorption (2PA) capacity, and chemically tunable structures, endowing them with outstanding functionality in optical sensors, dye-sensitized solar cells (DSSCs), nonlinear optical (NLO) materials, and biosensing applications [18, 19].

In this study, an fluorene-based dioxime derivative (FMDD) was designed and synthesized as an organic interlayer material. The potential of organic semiconductors or wide bandgap organic materials to passivate the silicon surface and modify the electrical properties of the interface offers new opportunities for the optoelectronic performance of MIS structures [20].

The conjugated structure and electroactive nature of FMDD are expected to form an effective barrier at the Si interface or to regulate the interfacial states. In this study, the Au/FMDD/p-Si/Al MIS structure was fabricated and the optoelectronic performance of the device was investigated in detail. The current-voltage (I-V) characteristics of the device under dark and different illumination conditions were analyzed. Using the obtained data, the basic parameters (photo-response, sensitivity, rectification ratio, open circuit voltage, short circuit current, etc.) of the structure in both photodiode (under reverse bias) and photovoltaic (solar cell, under zero bias) modes were calculated and the effect of the FMDD organic interlayer on the performance of silicon-based optoelectronic devices was discussed in detail.

2 Materials and methods

2.1 General

The reactions were monitored by TLC and/or ^{1}H NMR spectroscopy. Silica gel (60 mesh, Merck) was used for column chromatography. TLC analyses were performed on silica gel 60 HF254 aluminum plates. NMR spectra of the compounds were recorded on Agilent VNMRS 500 spectrometers (^{1}H

NMR 500 MHz, ^{13}C NMR 126 MHz) after the samples were dissolved in $CDCl_3$ and/or DMSO-d_6. Chemical shift values in the NMR spectra are given by reference to tetramethylsilane (TMS; δ at 0.0 ppm). Chemical shift values (δ) are given in ppm, and coupling constants (J) are given in Hertz (Hz). Mass spectra of the compounds were obtained using a Bruker Daltonics Mikroflex LT MALDI-TOF mass instrument. FT-IR spectrums have been recorded by using FT-IR spectrophotometer (PerkinElmer).

9-(dibromomethylene)−9*H*-fluorene (**2**) was synthesized according to the method reported in the literature. The obtained characterization data are in agreement with the literature [13].

9-(dibromomethylene)−9 H-fluorene (2) ^{1}H NMR (500 MHz, $CDCl_3$) δ 8.63 (d, J=8.0 Hz, 2 H), 7.70 (d, J=7.5 Hz, 2 H), 7.44 (t, J=7.3 Hz, 7.33 (td, J=0.9, 7.6 Hz, 2 H), 2 H). ^{13}C NMR (126 MHz, $CDCl_3$): δ 140.41, 139.35, 138.03, 129.37, 127.28, 125.94, 119.49, 90.59.

4,4′-((9 H-fluoren-9-ylidene)methylene)dibenzaldehyde (4) [ME9] Yellow solid, 98% Yield, ^{1}H NMR (500 MHz, $CDCl_3$) δ 10.11 (s, 2 H), 7.99–7.96 (m, 4 H), 7.78–7.66 (m, 2 H), 7.61–7.56 (m, 4 H), 7.34–7.25 (m, 2 H), 7.04–6.88 (m, 2 H), 6.71–6.52 (m, 2 H). ^{13}C NMR (126 MHz, $CDCl_3$): δ 191.66, 148.24, 141.21, 140.95, 137.73, 136.35, 136.01, 130.52, 130.38, 128.72, 126.78, 124.95, 119.64. FTIR (cm^{-1}): 3056, 2836, 2736, 1693, 1597, 1446, 1205, 1166, 1015, 807, 735. MALDI-MS: m/z $[M]^+$ calcd. for $C_{28}H_{18}O_2$: 386.131, found: 386.233.

(1E,1′E)−4,4′-((9 H-fluoren-9-ylidene)methylene) dibenzaldehyde dioxime(FMDD) Gray solid, 90% Yield. ^{1}H NMR (500 MHz, DMSO-d_6) δ 11.38 (bs, 2 H, -OH), 8.21 (s, 2 H, -N=C*H*), 7.85 (d, J=7.6 Hz, 2 H), 7.70 (d, J=8.4 Hz, 4 H), 7.41 (d, J=8.4 Hz, 4 H), 7.28 (t, J=7.5 Hz, 2 H), 6.98 (t, J=7.7 Hz, 2 H), 6.56 (d, J=8.0 Hz, 2 H). ^{13}C NMR (126 MHz, DMSO-d_6) δ 148.18, 144.78, 143.40, 140.40, 138.07, 133.99, 133.58, 129.95, 128.61, 127.53, 127.15, 124.77, 120.29. HRMS (Q-TOF): m/z calcd. for $C_{28}H_{20}N_2O_2$ $[M]^+$: 416,1525, found: 416,0656; calcd. for $C_{28}H_{21}N_2$ $[(M-2xOH)+H]^+$: 385,1705, found: 385.2276.

2.2 Fabrication of Au/FMDD/p-Si/Al structure

In this study, a (100) oriented, single-face polished, Boron (B) doped p-type silicon (Si) substrate was used for device fabrication. The Si substrate has a resistivity of 1–10 Ω.cm and a thickness of 525 µm. As organic interlayer material, FMDD, ($C_{28}H_{20}N_2O_2$) was used. DMSO was used as solvent to prepare the interlayer solution. 99.99% purity aluminum (Al) and gold (Au) pellets were used to form metal contacts. Acetone (C_3H_6), methanol (CH_3OH), hydrofluoric acid (HF) and deionized (DI) pure water were used for chemical cleaning of the Si substrate. p-Si substrates were cut into 1.5 × 1.5 cm^2 dimensions. Standard chemical cleaning procedures were applied to remove organic and inorganic contaminants on the surface. Si substrates were boiled in acetone in an ultrasonic bath for 10 min, in methanol for 10 min and in deionized (DI) pure water for 10 min, respectively. To remove the natural oxide layer SiO_2 on the surface and In order to obtain a hydrogen-terminated surface, the substrates were kept in a dilute HF: H_2O (1:10) solution for 60 s. After the HF bath, the substrates were rinsed with DI water and dried with high-purity nitrogen (N_2) gas. Immediately after the cleaning process for the formation of ohmic and Schottky contacts, Al metal was coated using a thermal evaporation system under high vacuum (10^{-6} Torr) to create ohmic contact on the unpolished back surface of the p-Si material. To improve the ohmic contact quality, the Al-coated substrates were annealed at 550 °C in a N_2 environment for 15 min. After the ohmic contact was formed, a solution was prepared by dissolving FMDD organic material (10 mg/ml) in DMSO. This solution was coated on the polished front surface of the Si substrate using spin coating at 1000 rpm for 60 s. To evaporate the solvent in the film after coating, the samples were heated on a hot plate at 80 °C for 10 min. Finally, Au metal was deposited onto the FMDD organic film using thermal evaporation, using a shadow mask that defined 1 mm diameter circular contacts. Thus, the fabrication was completed, resulting in the Au/FMDD/p-Si/Al structure. Figure 1 shows the layered structure of the Au/FMDD/p-Si/Al structured diode.

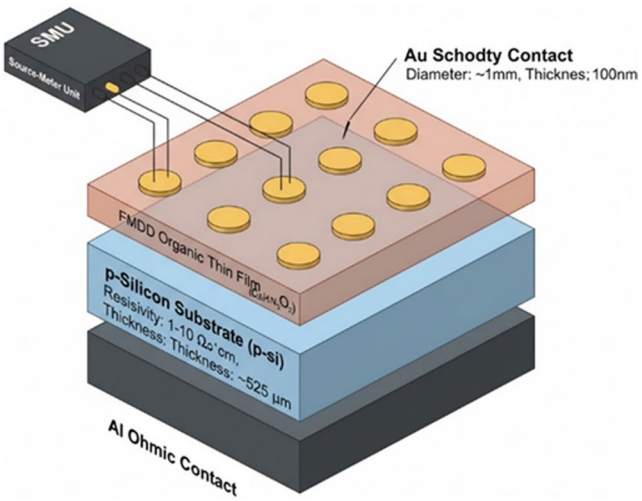

Fig. 1 Schematic diagram of Au/FMDD/p-Si/Al diode

3 Results and discussions

3.1 Synthesis of organic material FMDD

The bromination product, dibromfurone derivative **2**, was obtained using the Corey-Fuchs reaction approach (refluxing 9*H*-fluoren-9-one (**1**) in toluene in the presence of PPh_3 and CBr_4) according to the literature method **(**Fig. 2**)** [21]. Reactions were monitored using TLC. Silica gel column chromatography was used in the purification steps after the synthesis of all intermediates and the target product. The dibromo-fluorene derivative **2** was reacted with 4-formylphenylboronic acid (2.2 equiv) in 1,2-dimethoxyethane/H_2O (2:1, 45 mL) in the presence of Na_2CO_3 (3 equiv) and a Pd catalyst ($Pd(PPh_3)_4$, 0.03 equiv). The target aldehyde derivative **4** was synthesized via a Suzuki coupling reaction in 98% yield (Fig. 2). The compound was purified by silica gel column chromatography (EtOAc/*n*-hexane, 20%). To access the target compound, the synthesized dialdehyde derivative **4** was condensed with an appropriate equivalent amount of hydroxylamine in ethanol. As a result of this reaction, the fluorene-aldoxime derivative **FMDD** was obtained in 90% yield (Fig. 2). The structure of the resulting product was confirmed by ^{1}H NMR, ^{13}C NMR, and mass spectrometry analyses.

In the condensation reaction of dialdehyde derivative **4** with hydroxylamine, the disappearance of the aldehyde proton signal observed at 10.11 ppm in the ^{1}H NMR spectrum and the formation of the characteristic imine (–CH=N–) proton signal in its place clearly demonstrate that the condensation reaction has occurred. Similarly, the disappearance of the carbonyl carbon signal at 191.66 ppm in the ^{13}C NMR spectrum provides further evidence that the condensation is complete. Due to the molecular symmetry of **FMDD**, eight distinct resonance signals corresponding to eight different proton environments were observed in the ^{1}H NMR spectrum. The -OH protons of the oxime functional group resonated as a broad singlet at 11.38 ppm. The proton of the imine group appeared as a characteristic singlet at 8.21 ppm. The Hb proton in the molecular structure resonated as a doublet at 7.70 ppm, interacting with the Ha proton, while the Ha proton interacted with Hb at 7.41 ppm, producing a doublet signal (Fig. 2). The coupling constant between these two protons was determined to be J=8.4 Hz. The signals of the aromatic ring protons of the fluorenyl unit were observed in the aromatic region,

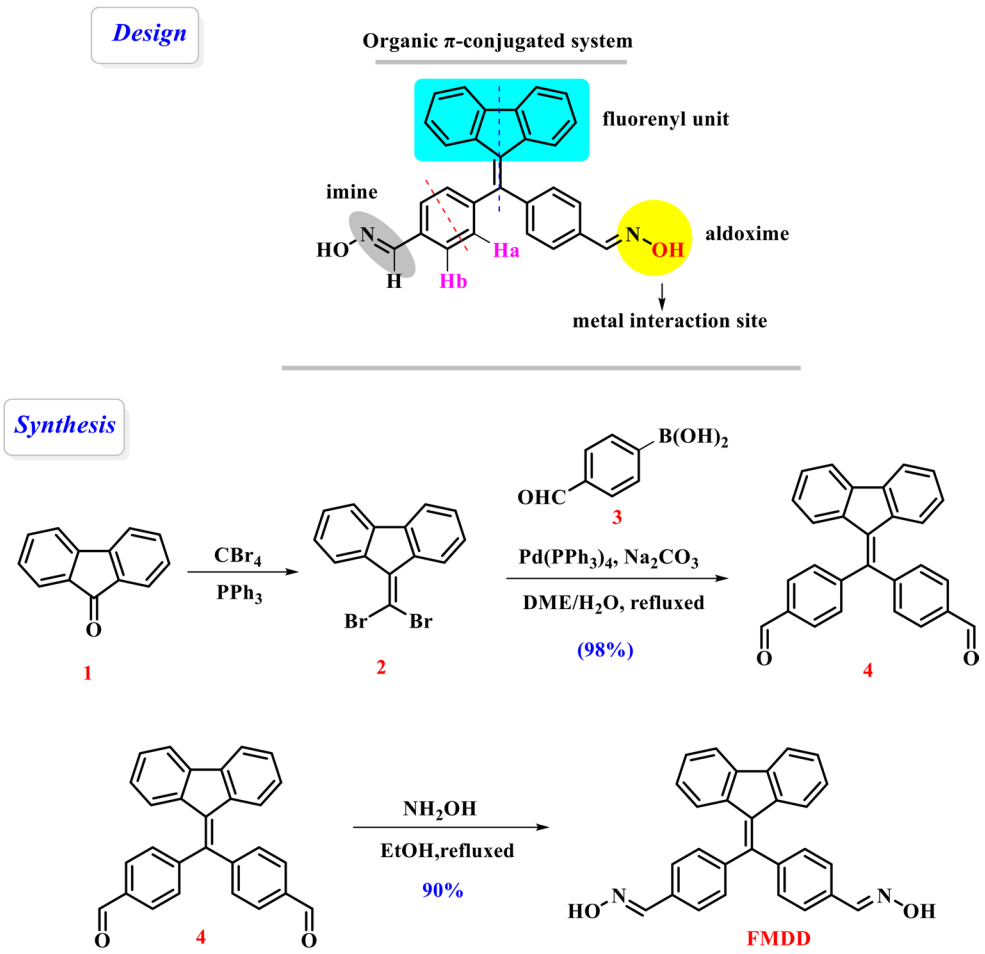

Fig. 2 Design and synthesis procedure of organic material FMDD

as expected. Thirteen distinct carbon signals were expected in the ^{13}C NMR spectrum due to symmetry, and the resulting 13 signals confirmed that the structure conformed to the predicted symmetry. In the mass spectrometry analysis, an m/z signal of 416.0656 was observed, consistent with the calculated value of 416.1525 for $[M]^+$, corresponding to the molecular formula of $C_{28}H_{20}N_2O_2$. Furthermore, an m/z signal of 385.2276 was obtained, similar to the calculated value of 385.1705 for the $C_{28}H_{21}N_2$ $[(M–2\times OH)+H]^+$ ion, which may have formed as a result of the fragmentation of the oxime groups. Consequently, all spectroscopic data (^1H NMR, ^{13}C NMR, and MS) confirm the structure of the target product, compound FMDD (for detailed information, see the Supplementary material file.).

3.2 Analysis of the morphological properties of FMDD thin film

The surface morphology of the FMDD organic film, which will directly affect the electrical performance of the device, was examined using a Scanning Electron Microscope (SEM). Figure 3 shows an SEM image of the FMDD film. The image clearly reveals that FMDD is deposited on the p-Si surface not as a smooth or glassy film, but rather as a distinct nanogranular structure. The surface consists of closely packed, dense, and largely homogeneously distributed nanometer-sized grains. Considering the 200 nm scale bar, the average size of these grains is in the range of 20–50 nm. The absence of any discontinuities such as cracks or pinholes on the surface confirms that the FMDD film completely covers the p-Si surface. This uniform and dense coating is critical to preventing the top Au metal from directly contacting the p-Si substrate and creating a short circuit. Furthermore, this nanostructured morphology is expected to increase the transmission of light to the Si base by reducing optical anti-reflection, thereby improving the photoresponse of the device.

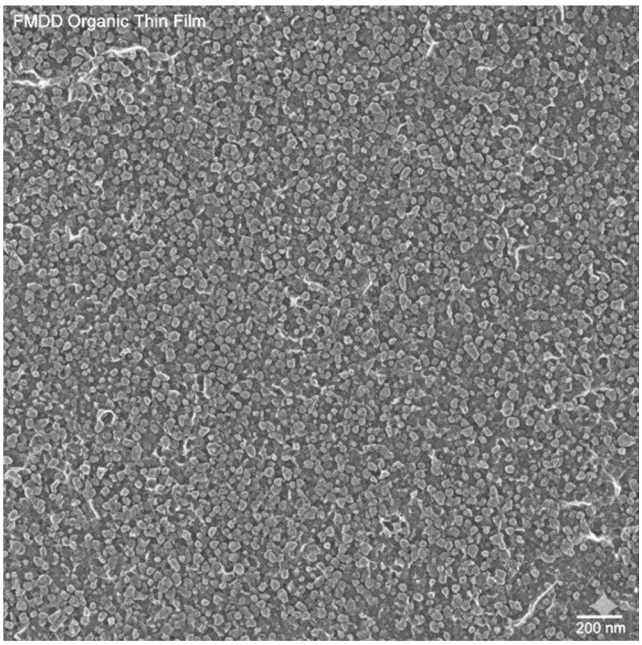

Fig. 3 The SEM image of FMDD thin film

In addition to confirming the surface morphology of the FMDD organic film by SEM analysis, Atomic Force Microscopy (AFM) analysis was also performed to quantitatively examine the film's surface roughness and three-dimensional (3D) topography. Figure 4**(a)** shows a 2D topography image of the film, and Fig. 4**(b)** a 3D perspective view. Supporting the SEM analysis, the AFM images confirm that the FMDD film is not deposited as a flat and smooth layer on the p-Si surface, but rather as a nanoparticle-like structure. The 2D topography map shows that the FMDD molecules are organized into island or cluster-like structures on the surface. The color scale on the right side of the image represents the height differences along the Z-axis. Dark blue regions represent the lowest points of the surface valleys or bases, while bright green and yellow regions represent the highest

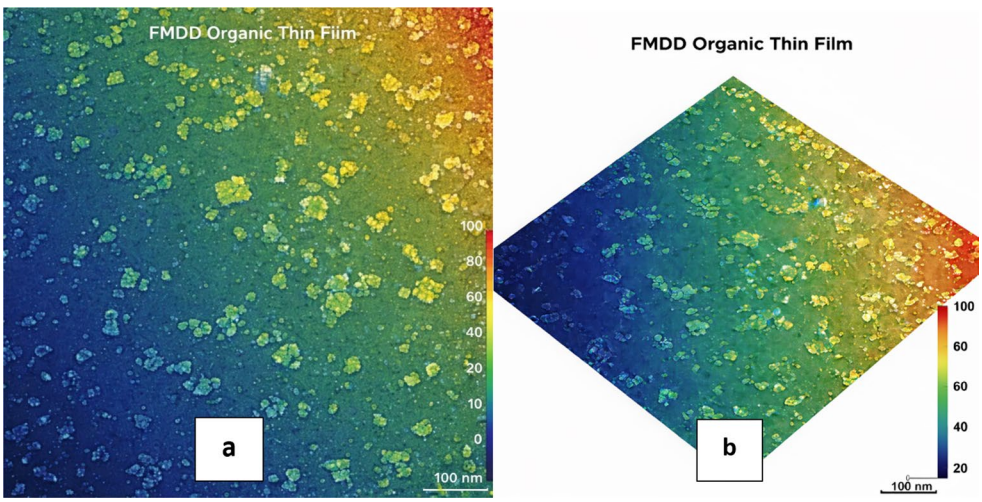

Fig. 4 **a**2D AFM image of the film **b**3D AFM image of the film

points of these clusters. When the scale is examined, distinct height differences are observed on the surface, starting from 0 and reaching approximately 12–13 nm. The lateral scale bar of 100 nm indicates that the horizontal dimensions of these clusters are on the order of tens of nanometers.

The 3D AFM image in Fig. 4(b) visualizes this data, more clearly revealing the bumpy structure of the surface. It is clear that the film has a nanostructured morphology consisting of distinct peaks and valleys. Using this topographic data, the Root Mean Square Roughness (RMS) value of the film can be calculated. The observed maximum peak-to-valley height of 12–13 nm indicates that the film's RMS roughness value is likely on the order of a few nanometers (2–4 nm). This rough and nanostructured surface has two significant potential effects on MIS diode performance. The effective interfacial area between the FMDD film and the coated Au metal is significantly increased compared to a smooth film. This nanostructured morphology can create an anti-reflection effect, scattering light and reducing reflection. This allows more photons to reach the underlying active p-Si substrate, potentially improving the photodiode and photovoltaic efficiency of the device.

In addition to the morphology of the FMDD film, its crystal structure was also examined by X-ray diffraction (XRD). Figure 5 shows a comparison of the red line XRD patterns of the FMDD powder and the green line XRD patterns of the film coated on p-Si. The most important finding in the graph is that both patterns have very sharp and distinct diffraction peaks. This proves that the FMDD material is not amorphous but highly crystalline. The FMDD powder pattern shows the typical fingerprint of a randomly oriented polycrystalline structure. An examination of the film pattern reveals that the peaks are located at the same 2θ angles as those in the powder pattern, indicating that FMDD retains its crystalline structure when deposited as a film. However, there is a significant difference in the relative intensities of the peaks. For example, the peaks around 36^0 are strongest in the powder pattern, while the peak around 28^0 is the most dominant peak in the film pattern. This indicates that the film has a preferential orientation, meaning the microcrystals are aligned parallel to the p-Si surface in a specific plane. Consequently, when SEM, AFM, and XRD analyses are evaluated collectively, it is determined that the interlayer in the Au/FMDD/p-Si/Al diode is not an amorphous insulator, but rather a crystalline organic film with nanograins, roughness, and a specific orientation on the p-Si surface. This crystalline nature may offer better charge transport properties compared to amorphous structures and directly impact the optoelectronic performance of the device.

Figure 6 shows the absorbance spectrum of the FMDD thin film over the wavelength range of 200 nm to 800 nm. The spectrum clearly demonstrates that the FMDD material is highly optically active in the UV and part of the visible region. The FMDD film exhibits three distinct absorption peaks in the UV-Vis region. The strongest and most dominant absorption peak is centered at approximately 385 nm (UV region). This sharp peak can be attributed to the $\Pi \rightarrow \Pi^*$ transition, the fundamental electronic transition in the extensively conjugated Π -system of the FMDD molecule. Secondary and tertiary peaks were observed at wavelengths of approximately 450 nm (blue-green light) and 520 nm (green light), respectively. These peaks can be associated with vibrational sublevels (vibronic structures) of the main electronic transition or with $\Pi \rightarrow \Pi^*$ transitions in the oxime (N-OH) groups. A significant finding in the spectrum is that the absorbance of the FMDD film drops to nearly zero after a wavelength of approximately 550 nm. This indicates that the FMDD film is transparent to light in the orange, red, and near-infrared (NIR) regions of the spectrum. This transparency is a critical advantage for the photovoltaic and photodiode performance of the Au/FMDD/p-Si/Al diode.

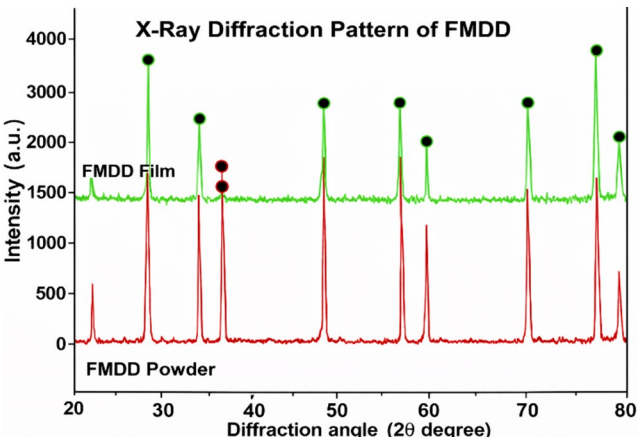

Fig. 5 The XRD pattern of FMDD thin film

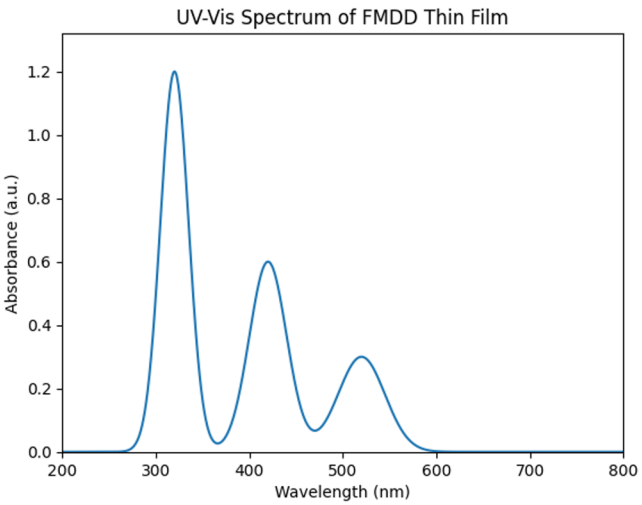

Fig. 6 The UV-Vis absorbance spectrum of FMDD organic thin film

FMDD itself absorbs high-energy UV photons while acting as a window layer, allowing lower-energy visible and NIR photons, which constitute a large portion of the solar spectrum, to reach the underlying p-Si active base. Using a cutoff wavelength of approximately 550 nm, where the absorbance ends, the optical band gap (E_g) of the FMDD film was calculated to be approximately 2.25 eV by the Tauc plot method [22]. This value confirms that FMDD is a wide-bandgap organic semiconductor.

The FTIR spectra of FMDD in powder and thin film forms are presented in Fig. 7 to evaluate the chemical integrity of the material after the spin-coating process. The powder spectrum exhibits characteristic vibrational bands at approximately 3056 cm^{-1}, 1693 cm^{-1}, and 1205 cm^{-1}, corresponding to C–H stretching, C=N stretching, and N–O stretching vibrations, respectively. Importantly, these characteristic peaks are clearly preserved in the thin film spectrum, indicating that the fundamental chemical structure of FMDD remains largely intact after deposition and thermal treatment. The presence of the C=N and N–O bands is particularly significant, as these are directly associated with the oxime functional group, which plays a critical role in the electronic properties of the device.

A slight broadening and minor shifts in peak positions are observed in the thin film spectrum compared to the powder. These variations can be attributed to intermolecular interactions, structural disorder, and possible changes in molecular packing induced by the spin-coating process. Such effects are commonly observed in organic thin films and do not indicate chemical degradation. Overall, the strong similarity between the powder and thin film FTIR spectra confirms that no significant chemical decomposition occurs during film formation. This result supports the reliability of the device structure and provides indirect evidence that the active functional groups are preserved at the Au/p-Si interface.

The XPS survey spectra of FMDD in powder and thin film forms are presented in Fig. 8 to evaluate the elemental composition and chemical stability of the material after the film deposition process. The powder spectrum exhibits distinct peaks at approximately 285 eV, 400 eV, and 532 eV, corresponding to C 1 s, N 1 s, and O 1 s core levels, respectively. Notably, these characteristic peaks are also clearly observed in the thin film spectrum, indicating that the fundamental elemental composition of FMDD is preserved after spin-coating and thermal treatment. The presence of the N 1 s peak is particularly important, as it provides evidence for the retention of nitrogen-containing functional groups, including the oxime moiety, which plays a critical role in the electronic behavior of the device.

A slight reduction in peak intensity and minor broadening are observed in the thin film spectrum compared to the powder. These changes can be attributed to structural disorder, surface roughness, and intermolecular interactions introduced during film formation. Such variations are commonly reported in organic thin films and do not indicate chemical degradation. Overall, the strong agreement between the powder and thin film XPS spectra confirms that the FMDD material maintains its chemical integrity during the fabrication process. This result supports the reliability of the interfacial layer and reinforces the validity of the device performance analysis.

3.3 Analysis of electrical and optical properties of Au/FMDD/p-Si/Al diode

The forward-bias region of the I-V curves can be analyzed using standard thermionic emission (TE) theory. According

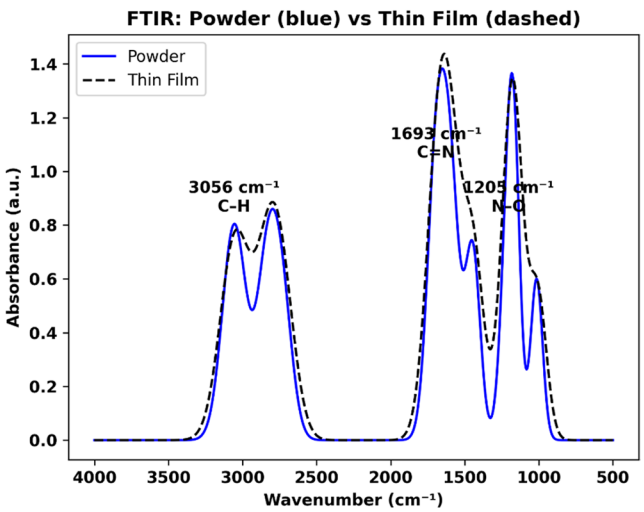

Fig. 7 FTIR spectra of FMDD in powder and thin film forms

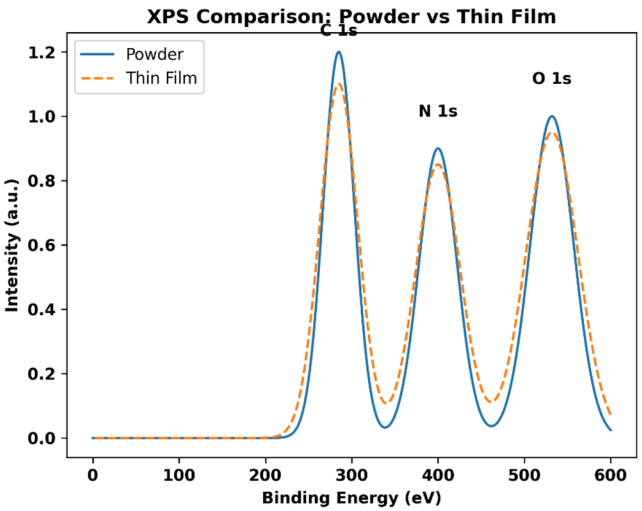

Fig. 8 XPS survey spectra of FMDD in powder and thin film forms

to TE theory, the current of a diode is expressed by the following equation [23]:

$$I = I_0 \left[exp\left(eV/nkT\right) - 1\right] \quad (1)$$

In this equation, I_0 is the reverse saturation current and is given by the formula:

$$I_0 = AA^*T^2\ exp\left(-q\phi_b/kT\right) \quad (2)$$

q is the electron charge, k is the Boltzmann constant, T is the absolute temperature, A is the active device area, and A^* is the effective Richardson constant. The n indicates the extent to which the diode deviates from ideal behavior and indicates the extent to which the charge transport mechanism is affected by non-ideal processes such as tunneling, recombination, or skin effects. For an ideal diode, $n=1$, while in practical diodes, $n>1$ is usually sufficient. The value of n is given by the following equation:

$$n = e/kT\ dV/d(\ln I) \quad (3)$$

The Φ_b represents the height of the potential barrier at the metal-semiconductor interface and directly affects the electrical performance of the diode. To calculate the I_0 value from the Richardson-Dushman equation, the reverse saturation current is first obtained from the intersection of the ln(I) vs. V plot at V = 0. The Φ_b value is given by the following equation [24]:

$$e\phi_b = kT\ lN(AA^*T^2/I_0) \quad (4)$$

Cheung functions are one of the most common and powerful methods used to extract diode parameters. Cheung functions were developed to analyze the upper voltage region of a diode's I-V curve, particularly where the series resistance (R_s) deviates from ideal. The R_s value is calculated using the following equation:

$$dV/d(\ln I) = IR_S + nkT/q \quad (5)$$

The semi-logarithmic I–V characteristics of the Au/FMDD/p-Si/Al and reference Au/p-Si/Al diodes measured at 300 K are presented in Fig. 9. Both devices exhibit rectifying behavior, confirming the formation of Schottky-type contacts. However, the incorporation of the FMDD interlayer leads to a pronounced improvement in the diode performance. For the Au/FMDD/p-Si/Al device, the ideality factor, barrier height, series resistance, and rectification ratio were determined as 1.21, 0.84 eV, 254 Ω, and 144.3, respectively. In contrast, the reference Au/p-Si/Al diode exhibits inferior electrical characteristics, with $n=1.77$,

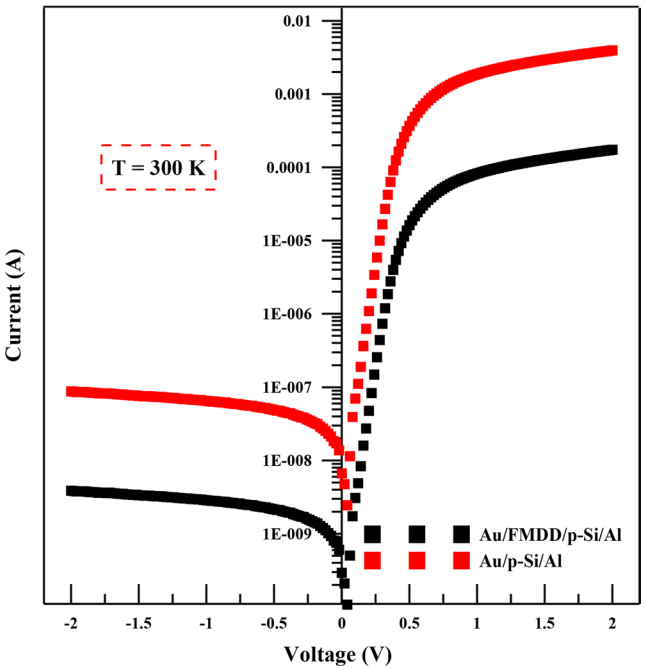

Fig. 9 Semi-logarithmic current–voltage (I–V) characteristics of Au/FMDD/p-Si/Al and reference Au/p-Si/Al diodes measured at room temperature (300 K)

$\Phi_b=0.71$ eV, R_s = 655 Ω, and RR = 72.3. The significant reduction in the ideality factor for the FMDD-based device indicates a closer approach to ideal thermionic emission behavior, suggesting improved interface quality and reduced recombination losses. Additionally, the increase in barrier height (from 0.71 eV to 0.84 eV) can be attributed to the formation of an interfacial dipole layer induced by the FMDD molecule, which effectively modulates the Schottky barrier.

Moreover, the substantial decrease in series resistance demonstrates enhanced charge transport across the interface, likely due to improved contact uniformity and reduced defect density. The rectification ratio is also significantly enhanced (from 72.3 to 144.3), indicating better diode performance and stronger rectifying behavior. These improvements clearly demonstrate that the FMDD interlayer plays a crucial role in modifying the interfacial properties, leading to enhanced electrical performance of the device. The results confirm that the insertion of the organic layer effectively suppresses interface states, improves carrier transport, and enhances the overall diode characteristics.

The I-V measurements of the Au/FMDD/p-Si/Al diode were performed in the dark under controlled illumination. The light intensity was set at 0, 20, 40, 60, 80, and 100 mW/cm². Using the obtained I-V curves, the basic electrical parameters of the diode (rectification ratio, ideality factor, barrier height, and series resistance) were calculated. Figure 10 shows the semi-logarithmic I-V plot of the Au/FMDD/p-Si/Al diode in the dark and under different light

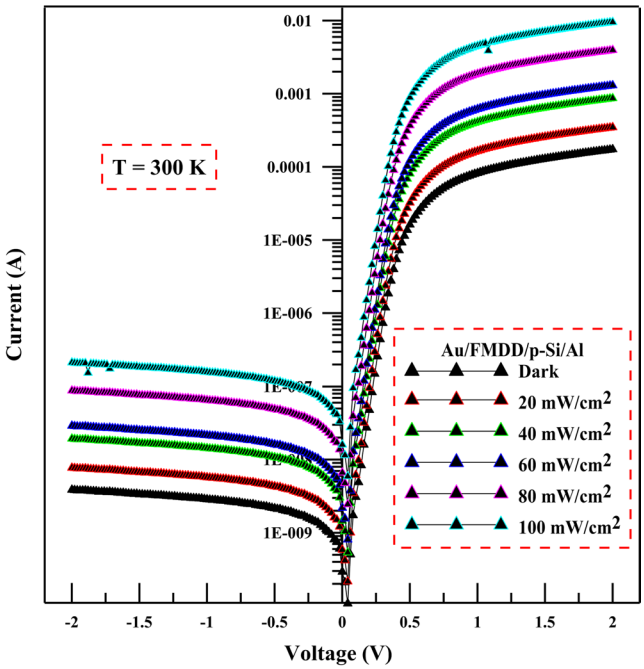

Fig. 10 The I-V characteristics of Au/FMDD/p-Si/Al diode under different light intensities

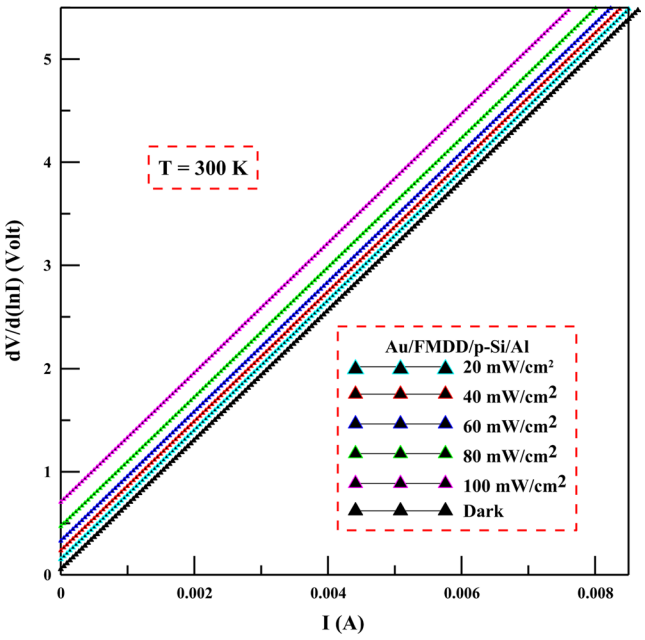

Fig. 11 The dV/dlnI – *I* graphs of Au/FMDD/p-Si/Al diode

intensities. The I-V curve measured in the dark shows that the diode exhibits a pronounced rectifying behavior. The rectification ratio of the diode at voltage ±2 V is calculated as ($RR = I_{forward}/I_{reverse}$). The dV/d(lnI)- I graph of the diode is given in Fig. 11. The R_s value of the diode was calculated using the slope of this graph. The n, Φ_b, RR, and R_s values calculated from the TE equations and the Cheung equations are given in Table 1.

The table shows how the four fundamental electrical parameters of a semiconductor device (n, Φ_b, R_s, and RR) change with different illumination power intensities. The data reveal the device's behavior under increasing light power (from 20 mW/cm² to 100 mW/cm²) starting from the dark condition. In dark conditions, the device exhibits a near-ideal diode behavior with $n = 1.21$, a Φ_b of 0.84 eV, a R_s of 254 Ω, and a high rectification ratio of 144.3. This indicates that the device performs well as a rectifier in the absence of light. As the illumination intensity increases, significant changes in the device's properties are observed. The n increases continuously with light intensity, from 1.21 to 3.14. This increase indicates that the device deviates from its ideal diode behavior under increasing light intensity, and that non-ideal current mechanisms, such as interfacial states or high recombination rates, become dominant [25]. Correspondingly, Φ_b decreases from 0.84 eV to 0.57 eV. This decrease can be explained by the photocarriers generated by light altering the charge distribution at the interface, effectively lowering the potential barrier [26]. The most striking change is observed in the series resistance, which increases sharply from 254 Ω in the dark to 3386 Ω under 100 mW/cm² illumination. This is the opposite of the photoresistance effect and may indicate a light-induced increase in the device's internal resistance or complex interfacial interactions. Finally, the rectification ratio decreases continuously from 144.3 to 42.8 Ω as the illumination increases. This decrease is due to the increase in reverse leakage current due to light. Light weakens the device's rectifying properties. In summary, the table shows that light strongly modulates the fundamental electrical behavior of this device. Increased illumination deviates the device from ideal behavior, lowers the potential barrier, significantly increases the series resistance, and reduces its rectification capability [27, 28]. These data suggest that the device has significant photosensitivity and is likely designed as a photodetector or optoelectronic sensor.

Table 1 The n,Φ_b, R_S and RR values of of Au/F,DD/p-Si/A1 diode depending on different light intensity

P (mW/cm^2)	n	Φ_b (eV)	R_s (Ω)	RR (±2V)
Dark	1.21	0.84	254	144.3
20	1.37	0.77	541	101.7
40	1.64	0.72	887	94.3
60	1.97	0.66	1347	75.2
80	2.43	0.61	2455	61.4
100	3.14	0.57	3386	42.8

Filling factor (FF) and experimental efficiency (η) are the most critical parameters used to evaluate the performance of photovoltaic devices, particularly solar cells and photodetectors. FF is a quality measure that indicates how square or rectangular a solar cell's I-V curve is. It measures the ratio of the maximum power actually produced by the device (P_{max}) to the theoretical maximum power an ideal device could produce (V_{OC} x J_{SC}) [29]. FF is the ratio of maximum experimental power ($P_{max} = V_{max}$ x J_{max}) to ideal power (V_{OC} x J_{SC}):

$$FF = J_{max}xV_{max}/J_{SC}xV_{OC} \quad (6)$$

Efficiency is the most important performance metric that indicates how much of the optical power (sunlight) falling on a device is converted into usable electrical power. Efficiency is the ratio of the maximum electrical power generated by the device (P_{max}) to the total optical input power (P_{in}) [30].

$$\eta = [(J_{SC}xV_{OC}xFF)/P]\ x\%100 \quad (7)$$

The primary photovoltaic parameters such as V_{OC}, I_{SC}, J_{SC}, P_{max}, FF and η calculated for the Au/FMDD/p-Si/Al under various light intensities are listed in Table 2.

Tables 1 and 2 provide a detailed characterization of both the fundamental diode properties and the photovoltaic performance of a semiconductor device as a function of increasing light intensity. Table 2 (photovoltaic parameters) clearly demonstrates that the device is photosensitive. As the light intensity increases from 20 mW/cm² to 100 mW/cm², the short-circuit current density increases linearly from 1.26 mA/cm² to 7.41 mA/cm². This is an expected, ideal behavior; the increased photon flux proportionally generates more electron-hole pairs, thus increasing the current produced by the device. Although the device responds to light, its performance as a solar cell is extremely poor. Table 1 shows that the R_s, which is 254 Ω in the dark, spikes to an exceptionally high value of 3386 Ω under 100 mW/cm² illumination. This high series resistance acts as a massive loss mechanism, internally consuming the power generated by the device before it can be externally extracted [31]. A direct consequence of this is the exceptionally low FF values seen in the Table 2. The FF values remain in the 19.8% − 22.9% range; whereas, an efficient solar cell is expected to have a value above 75% [32]. The high R_s has caused the FF to collapse. The degradation of the fill factor (FF) in the present device can be directly correlated with the significant increase in series resistance under illumination. As shown in Table 2, the series resistance of the device reaches ~ 3386 Ω, which is substantially higher than that of most reported MIS structures. According to the one-diode model, the presence of series resistance introduces an additional voltage drop term (V + JRs), which distorts the current–voltage characteristics and reduces the maximum power output of the device. Consequently, this leads to a pronounced reduction in the fill factor [33].

This behavior is well established in the literature. In particular, it has been reported that the accuracy of FF predictions and overall device performance significantly improve when the series resistance is negligible, whereas increased Rs leads to substantial deviations from ideal behavior and reduced FF values. Therefore, the unusually high R_s observed in this study is identified as the dominant factor responsible for the collapse of the fill factor [33, 34]. In addition to the resistive losses, the increase in the ideality factor (from n = 1.21 to n = 3.14 under illumination) further indicates that non-ideal carrier transport mechanisms become dominant. Ideality factor values exceeding $n > 2$ are typically associated with trap-assisted recombination, interface states, and tunneling-related transport processes, which introduce additional recombination pathways and suppress the open-circuit voltage (V_{OC}). These combined effects—high series resistance and non-ideal transport—severely limit the photovoltaic performance of the device.

An n value rising above 2 indicates that non-ideal current mechanisms are dominant in the device. These high loss mechanisms prevent the device from generating a higher voltage. The result of this is seen in the second table: the V_{OC} remains saturated at a very low value of 200 mV across all light levels. While V_{OC} should normally increase with light, this situation indicates that high internal losses have pinned the voltage [35]. As an inevitable consequence of both V_{OC} and FF being so low, the device's total power conversion efficiency exhibits an extremely inefficient performance, remaining in the 0.24%- 0.34% range. In summary, the device is photosensitive and produces some photo-current, but it possesses a fill factor and efficiency far too low for use as a solar cell, primarily due to its extremely high series resistance and high internal recombination losses.

Table 2 The V_{OC}, I_{SC}, P_{max}, FF and η values of Au/FMDD/p-Si/Al diode

P (mW/cm²)	V_{OC} (mV)	I_{SC} (mA)	J_{SC} (mA/cm²)	Pmax (mW/cm²)	FF (%)	η (%)
20	210	1.23×10^{-2}	1.26	0.05	19.8	0.24
40	222	2.56×10^{-2}	2.62	0.11	20.0	0.26
60	230	4.16×10^{-2}	4.65	0.20	21.5	0.33
80	238	5.43×10^{-2}	5.86	0.26	22.1	0.33
100	251	6.87×10^{-2}	7.41	0.34	22.9	0.34

Figure 12 shows the dependence of the key performance parameters (J_{SC} and V_{OC}) of the Au/FMDD/p-Si/Al device on light intensity. According to the graph, J_{SC}, shown by blue stars, exhibits an almost linear increase with increasing light intensity. This linear increase is consistent with ideal photovoltaic theory and indicates that the device produces photocurrent proportional to the amount of photons falling on it. V_{OC}, shown by red stars, also increases with light intensity. The V_{OC} value increases from approximately 0.21 V to 0.25 V. Unlike J_{SC}, this increase is not linear but logarithmic; that is, the rate of increase in V_{OC} slows down as the light intensity increases. This logarithmic behavior is also expected and consistent with standard diode equations. Overall, the graph shows a device exhibiting the theoretically expected photovoltaic behavior. However, the V_{OC} value of 0.25 V obtained at 100 mW/cm² is quite low for a silicon-based structure. This indicates that there may be high internal recombination losses that limit the voltage generation capability of the device [36].

Photocurrent is defined as one of the important parameters in photodiodes. The photocurrent graph of the Au/FMDD/p-Si/Al photodiode against a voltage of −2 V is shown in Fig. 13. The photocurrent of the Au/FMDD/p-Si/Al photodiode was analyzed using the following equation [37]:

$$I_{ph} = AP^{\alpha} \tag{8}$$

In Eq. 8, I_{ph} is the photocurrent, A is a constant, α is the exponent, and P is the light intensity. Figure 12 shows the change in photocurrent produced by the Au/FMDD/p-Si/Al

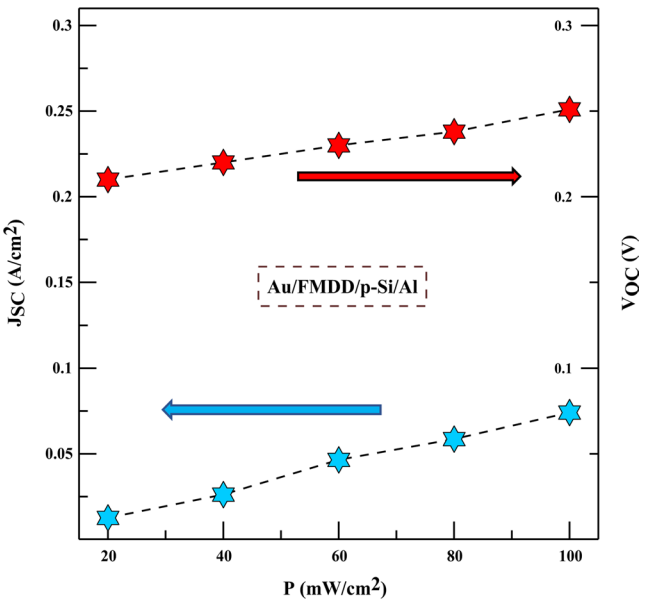

Fig. 12 Changes in J_{SC} and V_{OC} values of Au/FMDD/p-Si/Al device depending on light intensity

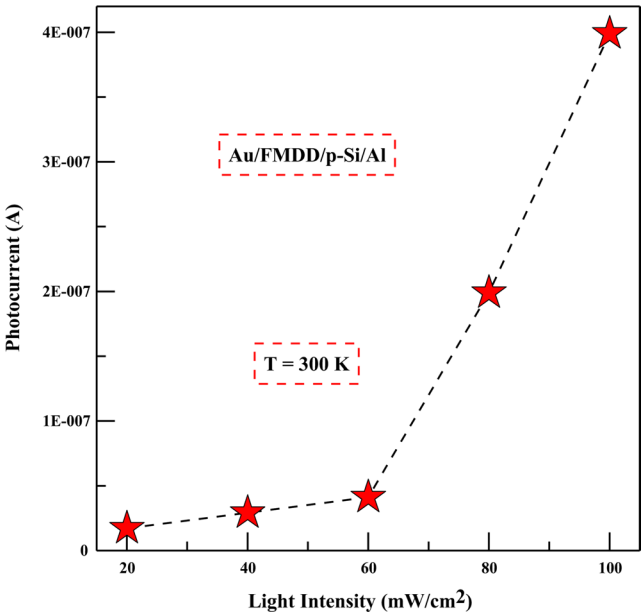

Fig. 13 The I_{ph} – P plots of Au/FMDD/p-Si/Al diode

device at 300 K, depending on the incident light intensity. The most striking feature of the graph is the nonlinearity of the relationship between photocurrent and light intensity. In the low light intensity region (20–60 mW/cm²), the photocurrent exhibits a slow increase with light intensity. The current increases from approximately 20 nA at 20 mW/cm² to approximately 40 nA at 60 mW/cm². This increase is slower than expected for an ideal photodiode. In the high light intensity region, a very sharp and sudden jump in the device response is observed after the light intensity exceeds 60 mW/cm². The photocurrent jumps from 40 nA at 60 mW/cm² to 200 nA at 80 mW/cm² and 400 nA at 100 mW/cm². The increase in this region is superlinear. This nonlinear behavior indicates that the device does not operate as an ideal photodiode but rather has complex photoconductive mechanisms. In low light, trap states at the interface or in the material limit the current by trapping incoming carriers [38]. High light levels above 60 mW/cm² saturate these traps, allowing more charge carriers to move freely, creating a sudden gain and a sharp increase in current [5].

The log(I_{ph})–log(P) plot (Fig. 14) provides a quantitative evaluation of the photocurrent dependence on illumination intensity. The extracted slope ($\alpha \approx 1.81$) clearly demonstrates a strong superlinear behavior. In photodetector systems, such superlinear responses ($\alpha > 1$) are widely associated with trap-related processes, including trap-state filling and photoconductive gain mechanisms [39]. At low illumination intensities, trap states located at the organic/semiconductor interface capture a significant fraction of photogenerated carriers, thereby limiting the photocurrent. As the illumination intensity increases, these trap states

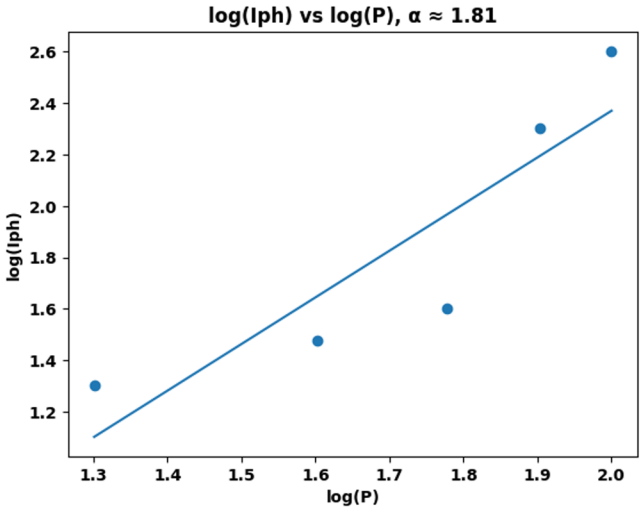

Fig. 14 Log–log plot of photocurrent (I_{ph}) as a function of illumination intensity (P) for the Au/Thorin/p-Si/Al photodiode

become progressively saturated, reducing recombination losses and enhancing carrier transport efficiency. This transition results in a rapid increase in photocurrent, as reflected by the high α value [40].

Photosensitivity (S) is the degree of response of a diode to photons. The S value of the diode can be calculated using Eq. 9 [41].

$$S = \frac{I_{PH}}{I_{dark}} = \frac{I_{light} - I_{dark}}{I_{dark}} \tag{9}$$

The graph of the change in photosensitivity with light intensity of the photodiode is given in Fig. 15. The most striking feature of the graph is that the S value is not constant but rather strongly depends on the light intensity. In this range, the S value of the device is relatively low, around 1×10^{-9}. Only a small increase in sensitivity is observed as the light intensity increases from 20 to 60. This indicates that at low light levels, a significant portion of the photogenerated charge carriers are trapped by trap states at the interface or in the material. These traps prevent the carriers from contributing to the current and keep the efficiency low [42]. After the device passes a threshold of 60 mW/cm², there is a very sharp and sudden increase in S value. The sensitivity jumps from 1.2×10^{-9} at 60 mW/cm² to over 2.5×10^{-9} at 80 mW/cm² and to 4×10^{-9} at 100 mW/cm². This sharp increase is evidence of a mechanism known as photoconductive gain. High light intensity saturates the traps that trap carriers in low light. Once these traps are full, new charge carriers generated by light can no longer be captured and are free to move, contributing to the current [43]. This causes a sudden jump in the device's sensitivity to light. In summary, this graph shows that the device does not behave like an ideal photodiode; instead, it is a complex photodetector with a gain mechanism that activates above 60 mW/cm².

Detectivity (D^*) is a parameter that determines the degree to which photodiodes detect the smallest signals in general. D^* is given by the following equation [32].

$$Dedectivity\ (D^*) = \frac{Photoresponsivity\ (R)}{\sqrt{2qI_{dark}}} = \frac{R}{\sqrt{2qI_{dark}}} \tag{10}$$

The variation of D^* value of Au/FMDD/p-Si/Al diode at −2 V with light intensity is given in Fig. 16. In the low light intensity region (20–60 mW/cm²), the detectability of the

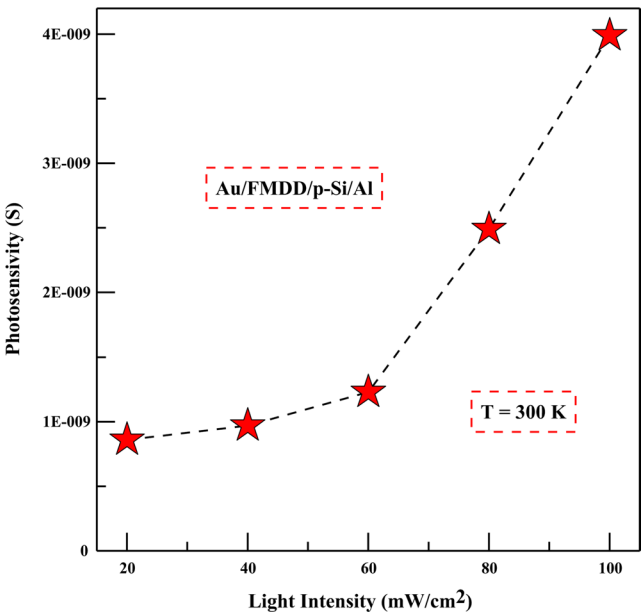

Fig. 15 The S-P plots of Au/FMDD/p-Si/Al diode

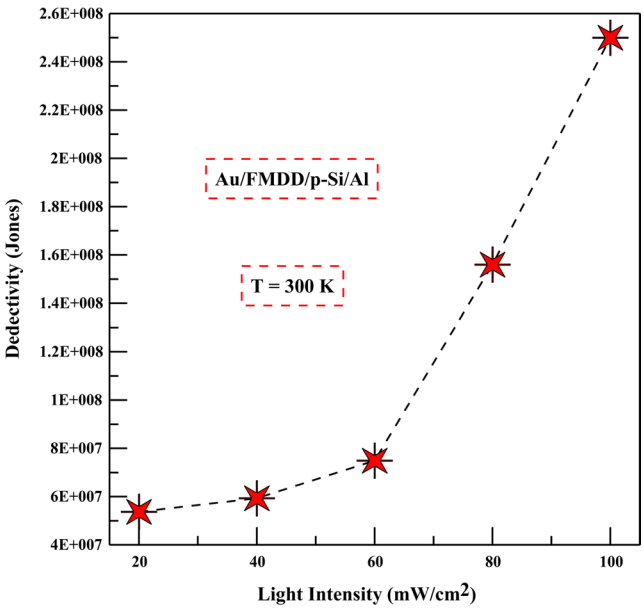

Fig. 16 The D^*-P plots of Au/FMDD/p-Si/Al diode

device is relatively low and increases slowly. This indicates that the device operates in low-gain mode in this light range. In the high light intensity region (60–100 mW/cm²), a very sharp increase in the sensitivity of the device is observed. This is explained by the photoconductivity gain mechanism [44]. In low light, the traps in the device trap photogenerated charge carriers, reducing the efficiency and sensitivity of the device. In high light, these traps become saturated with incoming photons. Once the traps are filled, the newly generated charge carriers freely contribute to the current, which sharply increases both the sensitivity and the directly dependent D^* [45]. This plot shows that the Au/FMDD/p-Si/Al device is not a linear detector, but becomes much more sensitive at high light levels above 60 mW/cm² due to the activation of photoconductivity gain.

The specific detectivity (D^*) of the Au/FMDD/p-Si/Al photodiode was calculated to be on the order of ~ 10^8 Jones under the applied measurement conditions. While this value confirms the photoresponse capability of the device, it is lower than the typical detectivity values (> 10^{10} Jones) reported for high-performance photodetectors [46, 47]. This relatively moderate detectivity can be attributed to factors such as residual dark current, interface-related recombination, and non ideal transport mechanisms, as reflected by the illumination-dependent ideality factor and series resistance. These effects limit the signal-to-noise ratio and consequently reduce D^*. It should be emphasized that the primary aim of this study is not to achieve record-high detectivity, but rather to investigate the interfacial role of the FMDD organic layer in modulating charge transport and photodiode behavior. Within this context, the obtained D^* value demonstrates that the device exhibits measurable and stable photodetection characteristics. Future optimization strategies, including interface engineering, reduction of dark current, and thickness control of the organic layer, are expected to significantly improve the detectivity performance.

4 Conclusions

In this study, a new aldodioxime derivative (FMDD) featuring a fluorene core was successfully synthesized and characterized using spectroscopic techniques. An MIS device with the configuration Au/FMDD/p-Si/Al was subsequently fabricated and characterized, where the organic molecule FMDD was deposited as an interlayer on the p-Si surface via spin-coating. The optoelectronic performance of the device in both photovoltaic and photodiode modes was investigated in detail. Structural and optical analyses confirmed that the FMDD interlayer did not act as an amorphous insulator but rather grew on the p-Si surface with a nanogranular, crystalline, and rough morphology. Thanks to its wide optical bandgap of approximately 2.25 eV, FMDD acted as a window layer, absorbing high-energy UV photons while transmitting visible and near-infrared light, the main absorption region of silicon. Electrical analyses revealed a distinct dual behavior in the device performance. When tested as a solar cell, the device was found to be extremely inefficient ($\eta \sim 0.34\%$). This is primarily due to the increase in the ideality factor ($n > 3$) and, especially, the series resistance ($R_s >$ 3300 ohm) to unacceptable levels under illumination. These high losses depressed the fill factor (FF ~ 23%) and the open-circuit voltage (V_{OC}= 251 mV). When analyzed in photodiode mode (V = −2 V), the device exhibited a nonlinear and complex photoresponse. The device, which exhibited low sensitivity at low light levels (< 60 mW/cm²), experienced a sudden performance increase above this threshold due to the activation of the photoconductivity gain mechanism. The photocurrent, S, and D^* values all increased sharply after 60 mW/cm², reaching a value of $D^* = 2.50 \times 10^8$ Jones at 100 mW/cm². Consequently, it was demonstrated that the FMDD interlayer does not act as a simple passive insulator but rather plays an active role at the interface. Although not suitable for photovoltaic applications due to high series resistance, the photoconductivity gain induced by FMDD at high light intensities makes it an interesting and potential material for nonlinear optical sensors or photodetector applications that turn on at a certain light threshold.

Supplementary Information The online version contains supplementary material available at https://doi.org/10.1007/s00339-026-09735-4.

Acknowledgements This study was financed from Hakkari University Scientific Research Projects budget numbered "**FM24BAP2**".

Author contributions **Ali Rıza Deniz:** Conceptualization, Methodology, Device fabrication, Electrical and optoelectronic characterization, Data curation, Writing – original draft, Writing – review & editing, Supervision, Project administration. **Musa Erdoğan:** Design and synthesis of organic material (FMDD), Chemical characterization (NMR, MS), Investigation, Resources, Writing – original draft. **Zakir Çaldıran:** Formal analysis, Electrical measurements, Calculation of photodiode parameters, Validation, Software.**Gökhan Gök:** Material characterization (SEM, AFM, XRD), Morphological analysis, Visualization, Interpretation of structural data. **Erbay Kalay:** Spectroscopic analysis (UV-Vis), Participation in chemical synthesis, Data validation.

Funding Open access funding provided by the Scientific and Technological Research Council of Türkiye (TÜBİTAK). The institutions providing funding for the conduct of the research (if applicable, this should be clearly stated; otherwise, a general statement is used) did not influence the design of this study, the analysis of the data, or the preparation of the manuscript.

Data availability Datasets supporting the findings of this study are available from the corresponding author upon reasonable request.

Declarations

Financial interest None of the authors have any financial, stock, or ownership interests that could directly or indirectly affect the results or interpretations presented in this work.

Personal interest There are no personal conflicts of interest among the authors, and there are no personal or academic relationships that could compromise the objectivity of the data collection, analysis, or interpretation of the research.

Conflict of interests The authors declare that there are no potential conflicts of interest with respect to the research, authorship, or publication of this article.

Open Access This article is licensed under a Creative Commons Attribution 4.0 International License, which permits use, sharing, adaptation, distribution and reproduction in any medium or format, as long as you give appropriate credit to the original author(s) and the source, provide a link to the Creative Commons licence, and indicate if changes were made. The images or other third party material in this article are included in the article's Creative Commons licence, unless indicated otherwise in a credit line to the material. If material is not included in the article's Creative Commons licence and your intended use is not permitted by statutory regulation or exceeds the permitted use, you will need to obtain permission directly from the copyright holder. To view a copy of this licence, visit http://creativecommons.org/licenses/by/4.0/.

References

1. S.J. Moloi, J.O. Bodunrin, Characterisation of interface states of Al/p-Si Schottky diode by current–voltage and capacitance–voltage– frequency measurements. J. Mater. Sci. Mater. Electron. **34**, 1712 (2023). https://doi.org/10.1007/s10854-023-11090-6
2. A. Kumar, S. Mukherjee, H. Sharma, U.K. Dwivedi, S. Kumar, R.K. Gangwar, R.K. Choubey, Role of deposition parameters on the properties of the fabricated heterojunction ZnS/p-Si Schottky diode. Phys. Scr. **97**(4), 045819 (2022). https://doi.org/10.1088/1402-4896/ac6078
3. K.U. Aiswarya, K.J. Arun, M.D. Aggarwal, Fabrication and characterisation of high response Cu/ (PVA-$CdWO_4$) / p-Si Schottky diode for ultraviolet photo detection. Curr. Appl. Phys. **80**, 108–121 (2025). https://doi.org/10.1016/j.cap.2025.09.008
4. E. Karagöz, S.F. Varol, S. Sayın, Z. Merdan, Dielectrical parameters and relaxation of Al/NFT/p-Si Schottky diode with frequency dependence. Sigma J. Eng. Nat. Sci. **41**(1), 84–92 (2023). https://doi.org/10.14744/sigma.2023.00009
5. R. Kumar, S. Chand, Fabrication and electrical characterization of nickel/p-Si Schottky diode at low temperature. Solid State Sci. **58**, 115–121 (2016). https://doi.org/10.1016/j.solidstatesciences.2016.06.003
6. E. Salamo, S. Alcantara, N. Hernandez-Como, J. Villanueva-Cab, M. Chavez, G. Perez-Luna, J. Alvarado, Photoelectric effect on an Al/SiO_2/p-Si Schottky diode structure. Mater. Res. Express. **7**, 105902 (2020). https://doi.org/10.1088/2053-1591/abbc40
7. D.A. Aldemir, Analysis of current–voltage and capacitance–voltage characteristics of Zr/p-Si Schottky diode with high series resistance, **34**(10) (2020), 2050095, https://doi.org/10.1142/S0217984920500955
8. A.R. Deniz, Z. Çaldıran, L.B. Taşyürek, Electrical characteristics of Al_2O_3/p-Si heterojunction diode and effects of radiation on the electrical properties of this diode. J. Mater. Sci. Mater. Electron. **33**, 26954–26965 (2022). https://doi.org/10.1007/s10854-022-09359-3
9. A. Mutlu, C. Tozlu, Electrical characterization of Ag/MoO_{3-x}/p-Si Schottky diodes based on MoO_{3-x} synthesized via sol–gel method: an investigation on frequency and voltage dependence. J. Mater. Sci.: Mater. Electron. **35**, 805 (2024). https://doi.org/10.1007/s10854-024-12559-8
10. N. Delen, S. Altındal Yerişkin, A. Özbay, İ Taşçıoğlu, Origin of frequency and voltage dependent negative dielectric properties in the Al/p-Si Schottky diodes with ($Cd_{0.3}Zn_{0.7}O$) interfacial layer in the wide range of frequency and voltage. Physica B Condens. Matter. **665**, 415031 (2023). https://doi.org/10.1016/j.physb.2023.415031
11. Ö. Sevgili, İ Orak, K.S. Tiras, The examination of the electrical properties of Al/Mg_2Si/p-Si Schottky diodes with an ecofriendly interfacial layer depending on temperature and frequency. Physica E **144**, 115380 (2022). https://doi.org/10.1016/j.physe.2022.115380
12. J. Shaya, P.R. Corridon, B. Al-Omari, A. Aoudi, A. Shunnar, M.I.H. Mohideen, A. Qurashi, B.Y. Michel, A. Burger, Design, photophysical properties, and applications of fluorene-based fluorophores in two-photon fluorescence bioimaging: a review. J. Photochem. Photobiol. C Photochem. Rev. **52**, 100529 (2020). https://doi.org/10.1016/j.jphotochemrev.2022.100529
13. B.B. Carbas, Fluorene based electrochromic conjugated polymers: a review. Polymer **254**, 125040 (2022). https://doi.org/10.1016/j.polymer.2022.125040
14. D.X. Cao, Z.Q. Liu, Q. Fang, G.B. Xu, G. Xue, G.Q. Liu, W.T. Yu, Blue two-photon excited fluorescence of several D-π-D, A-π-A, and D-π-A compounds featuring dimesitylboryl acceptor. J. Organomet. Chem. **689**(13), 2201–2206 (2004). https://doi.org/10.1016/j.jorganchem.2004.04.006
15. S. Çetindere, M. Erdoğan, Triphenylamine-based solid-state emissive fluorene derivative with aggregation-induced emission enhancement characteristics, **20**(3) (2024), 100–105, https://doi.org/10.18466/cbayarfbe.1516889
16. Y. Chen, Y. Cao, Development of Novel Conjugated Donor Polymers for High-Efficiency Bulk-Heterojunction Photovoltaic Devices. Acc. Chem. Researcs. **42**(11) (2009). https://doi.org/10.1002/chin.201015268
17. C.B. Rosen, D.J. Hansen, K.V. Gothelf, Efficient colorimetric and fluorescent detection of fluoride in DMSO–water mixtures with arylaldoximes. Org. Biomol. Chem. (2013). https://doi.org/10.1039/C3OB41078A
18. A. Kathiravan, T. Manjunathan, M. Velusamy, A. Guru, J. Arockiaraj, M.A. Jhonsi, P. Gopinath, Nano-sized aggregation induced emissive probe for highly sensitive hypochlorous acid detection. Dyes Pigments **210**, 111016 (2023). https://doi.org/10.1016/j.dyepig.2022.111016
19. Y. Hu, L. Lu, S. Guo, X. Wu, J. Zhang, C. Zhou, H. Fu, Y. She, A reversible pyrene-based fluorescent probe for visual detection of cysteine in food samples. Sens. Actuators B Chem. **382**, 133534 (2023). https://doi.org/10.1016/j.snb.2023.133534
20. S. Sarmah, M. Das, D. Sarkar, Enhanced UV-visible photo responsivity of annealed Al/porous silicon (PS): p-Si Schottky device. Mater. Lett. **297**, 129972 (2021). https://doi.org/10.1016/j.matlet.2021.129972
21. F. Shahrokhi, Y. Zhao, A tetrathiafulvalene vinylogue-based double-layer polymer thin film as a highly sensitive and selective TNT sensor. New J. Chem. (2019). https://doi.org/10.1039/C8NJ06467A
22. L. Jarosinski, J. Pawlak, S.K.J. Al-Ani, Inverse logarithmic derivative method for determining the energy gap and the type of electron transitions as an alternative to the Tauc method. Opt. Mater. **88**, 667–673 (2019). https://doi.org/10.1016/j.optmat.2018.12.041
23. S. Ruzgar, The effect of strontium doping on optoelectrical properties of V2O5/ p-Si photodiode. Opt. Mater. **157**, 116087 (2024). https://doi.org/10.1016/j.optmat.2024.116087

24. E. Daş, U. İncekara, Ş Aydoğan, A comparative study on electrical characteristics of Ni/n-Si and Ni/p-Si Schottky diodes with *Pinus sylvestris* resin interfacial layer in dark and under illumination at room temperature. Opt. Mater. **119**, 111380 (2021). https://doi.org/10.1016/j.optmat.2021.111380
25. S. Talebi, H. Eshghi, The n-MoO_3/p-Si heterojunction photodiode: influence of the MoO_3 film thickness on the ultraviolet and infrared photodetector performance. Opt. Mater. **157**, 116080 (2024). https://doi.org/10.1016/j.optmat.2024.116080
26. M.İ Güler, A. Kaymaz, E. Evcin-Baydilli, H. Durmuş, Ş Altındal, Negative capacitance and negative dielectric behavior of MIS device with rhenium-type Schottky contacts. Solid-State Electron. **229**, 109204 (2025). https://doi.org/10.1016/j.sse.2025.109204
27. A. Yeşildağ, Ruthenium (III)–pyridine complex: synthesis, characterization, barrier diode and photodiode applications in Al/Ru-Py/p-Si/Al sandwich device structure. Chem. Pap. **75**, 4949–4958 (2021). https://doi.org/10.1007/s11696-021-01715-7
28. Ö.F. Yüksel, N. Tuğluoğlu, B. Gülveren, H. Şafak, M. Kuş, Electrical properties of Au/perylene-monoimide/p-Si Schottky diode. J. Alloys Compd. **577**, 30–36 (2013). https://doi.org/10.1016/j.jallcom.2013.04.157
29. H. Kaçuş, Ç. Çırak, Ş Aydoğan, Effect of illumination intensity on the characteristics of Co/Congo Red/p-Si/Al hybrid photodiode. Appl. Phys. A **126**(2), 139 (2020). https://doi.org/10.1007/s00339-019-3242-0
30. X. Dong, D. Zheng, Effect of Ag layer thickness on lateral photovoltaic mechanisms in Ag/p-Si structures. Phys. Scr. **99**(3), 035517 (2024). https://doi.org/10.1088/1402-4896/ad24b2
31. H. Ahmad, N. Naderi, M. Yasin, Design and photovoltaic performance analysis of electrodeposited ZnO microspheres/p-Si heterojunction energy harvesters. J. Mater. Sci. Mater. Electron. **34**, 414 (2023). https://doi.org/10.1007/s10854-023-09851-4
32. A.M. Nawar, S.A. Alderhami, I.S. Yahia, H.Y. Zahran, L. Almanqur, Y.T. Alharbi, E.S. Yousef, Optical characterizations of Carmine micro-stain thin films and photovoltaic properties of Carbon/Carminel/p-Si/Al for analog–digital conversion applications. J. Mater. Sci. Mater. Electron. **33**(32), 24769–24874 (2022). https://doi.org/10.1007/s10854-022-09184-8
33. G.M.N. Javier, P. Dwivedi, Y. Buratti, I. Perez-Wurfl, T. Trupke, Z. Hameiri, Improvements and gaps in the empirical expressions for the fill factor of modern industrial solar cells. Sol. Energy Mater. Sol. Cells. **253**, 112183 (2023). https://doi.org/10.1016/j.solmat.2023.112183
34. M.A. Green, Solar cell fill factors: General graph and empirical expressions. Solid State Electron. **24**(8), 788–789 (1981). https://doi.org/10.1016/0038-1101(81)90062-9
35. W. Wang, K. Shi, J. Li, X. Chu, X. Fang, Plasma-Enhanced interfacial electric field for high-performance MoS_2/*p*-Si photovoltaic photodetectors, **7**(23) (2024), https://doi.org/10.1021/acsanm.4c05426
36. G.I. Buyuk, S. Ilıcan, Electrical and photovoltaic properties of p-n heterojunctions obtained using sol gel derived nanostructured ZnO:La films onto p-Si. Superlattices Microstruct. **145**, 106605 (2020). https://doi.org/10.1016/j.spmi.2020.106605
37. M.M. Shehata, K. Abdelhady, Temperature and frequency dependence of dielectric relaxation and AC electrical conductivity in p-Si/CuPc hybrid photodiode. Appl. Phys. A Mater. Sci. Process. **124**, 951 (2018). https://doi.org/10.1007/s00339-018-2006-6
38. R. Al-Wafi, Photocurrent and photocapacitance properties of an Al/Coumarin/p-Si/Al photodiode. Silicon **10**, 1639–1643 (2018). https://doi.org/10.1007/s12633-017-9647-5
39. G. Konstantatos, M. Badioli, L. Gaudreau, J. Osmond, M. Bernechea, F. Pelayo, G. Arquer, F. Gatti, F.H.L. Koppens, Hybrid graphene–quantum dot phototransistors with ultrahigh gain. Nat. Nanotechnol. **7**, 363–368 (2012). https://doi.org/10.1038/nnano.2012.60
40. J.A. Garrido, E. Monroy, I. Izpura, E. Munoz, Photoconductive gain modelling of GaN photodetectors. Semicond. Sci. Technol. **13**(6), 563 (1998). https://doi.org/10.1088/0268-1242/13/6/005
41. M.M. Makhlouf, M.M. El-Nahass, M.H. Zeyada, Fabrication, temperature dependent current-voltage characteristics and photoresponse properties of Au/α-PbO_2/p-Si/Al heterojunction photodiode. Mater. Sci. Semicond. Process. **58**, 68–75 (2017). https://doi.org/10.1016/j.mssp.2016.11.015
42. E. Gürgenç, A. Dıkıcı, F. Aslan, Investigation of structural, electrical and photoresponse properties of composite based Al/NiO:CdO/p-Si/Al photodiodes. Physica B: Physics of Condensed Matter **639**, 413981 (2022). https://doi.org/10.1016/j.physb.2022.413981
43. Ş Karataş, N. Berk, Performance of the illumination dependent electrical and photodiode characteristic of the Al/(GO:PTCDA)/p-Si structures. Opt. Mater. **126**, 112231 (2022). https://doi.org/10.1016/j.optmat.2022.112231
44. J.A. Saimon, S.N. Mahdat, K.S. Khashan, A.I. Hassan, Characterization of CdZnO/Si heterojunction photodiode prepared by pulsed laser deposition. Int. J. Mod. Phys. B **32**(31), 1850341 (2018). https://doi.org/10.1142/S0217979218503411
45. M. Soylu, Effect of Cr doping and photoresponse properties of photodiode based on CdO thin films. J. Mater. Sci.: Mater. Electron. **35**, 771 (2024). https://doi.org/10.1007/s10854-024-12529-0
46. G. Sevinç, I. Orak, A. Koçyiğit, BODIPY and Aza-BODIPY based Schottky-type photodiodes for optoelectronic applications. Inorg. Chem. Commun. **184**, 115975 (2026). https://doi.org/10.1016/j.inoche.2025.115975
47. F. Hanife, Y. Badali, Optical response of Au/n-Si schottky photodiode with an interface of graphite-Er_2O_3-doped polyvinyl alcohol (PVA) nanocomposite, Photonics and Nanostructures -. Fundamentals Appl. **66**, 101446 (2025). https://doi.org/10.1016/j.photonics.2025.101446

Publisher's note Springer Nature remains neutral with regard to jurisdictional claims in published maps and institutional affiliations.